Magnetic Resonance Imaging, Vol. 15, No. 6, pp. 679–688, 1997
Copyright © 1997 Elsevier Science Inc.
Printed in the USA. All rights reserved
0730-725X/97 $17.00 + .00

ELSEVIER

PII S0730-725X(97)00033-7

● *Original Contribution*

WATERSHED-BASED SEGMENTATION OF 3D MR DATA FOR VOLUME QUANTIZATION

J. SIJBERS,* P. SCHEUNDERS,† M. VERHOYE,‡ A. VAN DER LINDEN,‡
D. VAN DYCK† AND E. RAMAN*

*Biomedical Physics, †Vision Lab, and ‡Bio-Imaging Lab, Department of Physics, University of Antwerp,
Groenenborgerlaan 171, 2020 Antwerpen, Belgium

The aim of this work is the development of a semiautomatic segmentation technique for efficient and accurate volume quantization of Magnetic Resonance (MR) data. The proposed technique uses a 3D variant of Vincent and Soilles immersion-based watershed algorithm that is applied to the gradient magnitude of the MR data and that produces small volume primitives. The known drawback of the watershed algorithm, oversegmentation, is strongly reduced by a priori application of a 3D adaptive anisotropic diffusion filter to the MR data. Furthermore, oversegmentation is a posteriori reduced by properly merging small volume primitives that have similar gray level distributions. The outcome of the preceding image processing steps is presented to the user for manual segmentation. Through selection of volume primitives, the user quickly segments the first slice, which contains the object of interest. Afterwards, the subsequent slices are automatically segmented by extrapolation. Segmentation results are contingently manually corrected. The proposed segmentation technique is tested on phantom objects, where segmentation errors less than 2% are observed. In addition, the technique is demonstrated on 3D MR data of the mouse head from which the cerebellum is extracted. Volumes of the mouse cerebellum and the mouse brains in toto are calculated. © 1997 Elsevier Science Inc.

Keywords: **3D segmentation; Watershed algorithm; Volume quantization; MR Imaging.**

INTRODUCTION

In many image processing tasks, segmentation is an important step toward the analysis phase. It allows quantification and visualization of the objects of interest. Recently, image segmentation methods were extensively reviewed by Clarke et al.[1] They concluded that segmentation of medical images is still a difficult task and fully automatic segmentation procedures are far from satisfying in many realistic situations. When the intensity or structure of the object differs significantly from the surroundings, segmentation is obvious. In all other situations manual tracing of the object boundaries by an expert seems to be the only "valid truth" but it's undoubtedly a very time-consuming task.

On MR data, fully automatic image segmentation techniques have been developed that can be subdivided in two major classes: gray scale single image segmentation and multispectral segmentation. Regarding the first class, the most intuitive approach is the threshold-based segmentation method where the threshold is chosen globally[2,3] or locally.[4] The method is restricted to relative simple structures and is hindered by variability of anatomical structures as well as image artefacts. Other approaches make use of edge detection for image segmentation.[5,6] These, however, suffer from over- or undersegmentation, induced by improper threshold selection.[7] In addition, the edges found are usually not closed such that edge linking techniques are further required. Concerning the multispectral class, segmentation techniques using clustering techniques like k-means clustering,[8] adaptive hierarchical clustering,[9,10] fuzzy k-means,[11] etc., are applied.[12] Like all unsuper-

---

Address correspondence to Jan Sijbers, University of Antwerp, RUCA, Groenenborgerlaan 171, B-2020 Antwerpen, Belgium.

vised segmentation techniques, multispectral data analysis is fully automatic and superior in reproducibility, but it can only be exploited when the MR characteristics of the object of interest differ significantly from those of the surrounding structures.

On the other hand, results of supervised segmentation are less reproducible but the segmentation process can be controlled by the operator. We choose for a semiautomatic single image segmentation procedure for 3D MR images in which user interaction is allowed to control the segmentation process and in which data is preprocessed as far as possible such that the posterior user-interaction time is strongly reduced.

The first preprocessing step concerns reduction of random noise, as segmentation results are usually highly dependent on image noise. This is because noise tends to dislocate edges and hampers the detection of fine image detail. In this article we demonstrate the effect of random noise reduction. Apart from random noise, structured noise, for example, due to magnetic field inhomogeneities, may degrade the image as well.[13] However, this type of noise was not observed to significantly pollute our data and is further not discussed in this article. However, it must allways be kept in mind that this type of noise may influence the volume quantification results.

Among the vast amounts of noise filtering schemes already available in the literature, the filter that best serves the posterior segmentation method is selected. The most common noise reduction technique is time averaging, with the major advantage that SNR is increased while the spatial resolution remains intact, provided a stationary imaging process. While this approach is quite time consuming and, hence, almost impossible in case of conventional 3D MR imaging, time averaging is usually replaced by spatial averaging. Wang and Lei[14] justified the heuristics that an MR image can be regarded as consisting out of many regions in which the signal is stationary, has a Gaussian probability density function and is ergodic in the mean and variance. The mean ergodic property justifies the use of spatial averaging within those regions to estimate the pixel expectation value. The main problem is to find these stationary regions. In conventional lowpass filtering,[15,16] these filters act in the Fourier space where all local spatial coherence is lost. As a consequence, although SNR increases significantly and is able to reduce Gibbs ringing artefacts, spatial resolution is severely degraded.[17] Recently, wavelet analysis[18] is designed to overcome this and is quite effective in noise reduction and edge enhancement. However, the reported findings also indicate that some local edge artefacts are introduced.[19] The problem of finding the proper area for spatial averaging is partly solved by the so-called sigma filters,[20] where spatial averaging is halted as soon as strong image gradients are detected.[21] A more elaborated approach can be found in the work of Perona et al.,[22] who developed an anisotropic diffusion scheme for image data where the diffusion and flow functions are guided by local gradient strengths in different directions. The properties of Perona's filter are: (1) efficient noise removal in homogeneous regions, (2) preservation of object boundaries, and (3) edge sharpening. This filtering technique was successfully applied to 2D and 3D MR data by Gerig et al.[23] Although the performance of the noise filter is excellent, the underlying image model is a piecewise constant or slowly varying one. As a result, the edge sharpening causes a region with a constant grey-value slope to be broken up in constant plateaus. The edge sharpening property is not retained in the approach of Yang et al.[24] In his article he also proposed a more robust way of measuring the anisotropy of the local structure.[25]

We adopted the last filter because it smooths out homogeneous regions while retaining the edge information in an anisotropic manner, which is indispensable for accurate image segmentation. In the following section this filtering technique is reviewed and an extension to 3D is presented. The anisotropic filter is applied to combat oversegmentation of the data. In Experiments and Discussion we will demonstrate the influence of this filter on the final segmentation results.

The actual segmentation technique starts with a subdivision of the data in basic volume elements, called catchment basins by application of a watershed algorithm to the gradient magnitude of the original 3D data set. Among several existing algorithms, the immersion-based approach of Vincent and Soilles[26] was used because of its accuracy and speed of computation.[27] The technique is based on the assumption that image contours correspond to the crest lines of the gradient magnitude image that can be detected via watershed tracing. The output of the watershed algorithm is a partitioning of the input data in volume regions of which the interior does not contain any sharp gray value transitions. Without preprocessing of the data, the algorithm leads inevitably to an oversegmentation of the data because all the crest lines of the data set are detected. Therefore, the adaptive anisotropic filter,[24] mentioned above, is a priori applied to the image data.

Afterwards, oversegmentation is additionally reduced by merging basic volume elements. A 2D merging scheme was suggested by Maes et al.[28] who used the Minimum Description Length Principle[29-31] to deal with the oversegmented output of the watershed algorithm. Thereby, the description length, i.e., the number of bits to encode each region primitive, was calculated.

For the interior an entropy criterion was used while the boundary was encoded by chain coding. Regions are merged when the total description length gain is positive. However, problems arise because not all regions can uniquely be chain coded. Moreover, extension to 3D using this criterion is not possible, as the boundary surface cannot uniquely be determined in the same way as was done in 2D. Also, for calculation of the entropy, the probability density function of the basic volume element is required. Thereby, the unknown distribution is usually estimated by convolving the original histogram with a Gaussian Parzen window.[32] However, because of the high number of basic volume elements, the convolution with each histogram would severely slow down the merging process.

We propose an alternative merging scheme based on hypothesis testing that is not dimension restricted and computationally far less complex. Thereby, small volume primitives are merged with the most similar neighboring region. In this way, the number of basic volume elements is significantly reduced, such that user interaction time during the posterior semiautomatic segmentation is strongly minimized.

All preprocessing steps are fully automatic. The final extraction of the object of interest takes place in the last part. The first slice is manually segmented, after which all subsequent slices are automaticaly segmented. Each segmentation result is eventually manually corrected by the user.

The accuracy of the presented volume quantization method is in a first phase tested on phantom objects with known volumes. In addition, the segmentation technique is applied to 3D MR data of the mouse head. It has been reported that the vermis of the cerebellum is smaller in human fragile X patients than in controls.[33] (The fragile X syndrome is caused by mutations in the fragile X gene FMR1. It is the most common cause of developmental disability.) Similar observations were made on patients with autism from 2D Magnetic Resonance scans[34] and on mice with the fragile X syndrome from 2D micrographs of histologic slices.[35] The authors reported volume measurements obtained from invasive techniques (slicing of the fixated mouse head) where errors of more than 10% are common. 3D MR imaging and processing enable the study of physiological structures without destroying the object. The 3D information present in the MR data can fully be exploited for image processing and analysis. In addition, the nondestructive character of MR imaging allows in vivo study of the object of interest and, hence, allows the study of time-dependent processes. As an application, the volume of both cerebellum and the total mouse brains is quantized from the segmentation output. Finally, 3D reconstructions from the segmentation results are shown.

ADAPTIVE ANISOTROPIC DIFFUSION FILTER

In the following, we review the adaptive anisotropic diffusion filter and present an extension to 3D. Suppose $f(\vec{r})$ is a 3D image where $\vec{r} = (x_1, x_2, x_3)$ is a three-dimensional position vector. The filtering process consists of convolving $f(\vec{r})$ with a Gaussian kernel $h(\vec{r})$ of which the shape is pointwise adapted to the local structure within a neighborhood Ω. The resulting filtered function $g(\vec{r})$ can be written as follows:

$$g(\vec{r}_0) = \frac{\iiint_\Omega h(\vec{r}_0 - \vec{r}) f(\vec{r}) d\vec{r}}{\iiint_\Omega h(\vec{r}_0 - \vec{r}) d\vec{r}} \quad (1)$$

where

$$h(\vec{r} - \vec{r}_0) = \exp\left[-\frac{1}{2} \sum_{i=1}^{3} \frac{((\vec{r} - \vec{r}_0) \cdot \vec{n}_i)^2}{\sigma_i^2(\vec{r}_0)} \right] \quad (2)$$

In Eq. (2), the vectors $\vec{n}$ are the eigenvectors of the 3×3 second moment matrix R of the Fourier spectrum $|F(u)|^2$. The coefficients of R can as well be calculated in the spatial domain:

$$R_{ij} = \iiint_\Omega u_i u_j |F(u_1, u_2, u_3)|^2 du_1 du_2 du_3 \quad (3)$$

$$= \frac{1}{(2\pi)^3} \iiint_\Omega \left(\frac{\partial f}{\partial x_i}\right)\left(\frac{\partial f}{\partial x_j}\right) dx_1 dx_2 dx_3 \quad (4)$$

where $i, j = 1, 2, 3$. R is positive semidefinite and Hermitian, hence having only positive eigenvalues. The direction of the eigenvector $\vec{n}_1$, corresponding to the smallest eigenvalue, say λ_1, determines the main direction of the pattern in the neighborhood Ω of the spatial domain. Alternatively, the three eigenvalues λ_1, λ_2, and λ_3, with $\lambda_1 \leq \lambda_2 \leq \lambda_3$, determine the relative orientation of the pattern in the respective directions.

The shape of the kernel h [see Eq. (2)] is controlled by the standard deviations σ_1, σ_2, and σ_3, which are functions of the local gradient strength in the respective directions. From the eigenvalues anisotropy measures are derived that are used to design the standard deviations:

$$a_{12} = \frac{\lambda_2 - \lambda_1}{\sum_i \lambda_i} \text{ and } a_{13} = \frac{\lambda_3 - \lambda_1}{\sum_i \lambda_i} \quad (5)$$

The standard deviations should be large along the main direction(s) of the pattern such that data is only smoothed in homogeneous regions and along instead of across edge surfaces.

In addition, corners should be preserved during filtering. A corner is identified as a situation where the pattern is relative isotropic ($a_{12} \approx 0$; $a_{13} \approx 0$) while the local gradient strength $|\nabla f(\vec{r})|^2$ is large. Therefore, a spatial-dependent corner strength C is defined as:

$$C(\vec{r}) = (1 - a_{12} - a_{13})|\nabla f(\vec{r})|^2 \qquad (6)$$

From Eq. (5) and Eq. (6), the standard deviations are designed as follows:

$$\sigma_1(\vec{r}) = \frac{\sigma}{1 + C(\vec{r})} \quad \sigma_2(\vec{r}) = \frac{\sigma(1 - 2a_{12})}{1 + C(\vec{r})}$$

$$\sigma_3(\vec{r}) = \frac{\sigma(1 - a_{12} - a_{13})}{1 + C(\vec{r})} \qquad (7)$$

σ stands for the standard deviation of the image noise. This parameter may be determined in several ways.[36] It can be measured by acquiring two images of the same object, subtracting one from the other and finding the standard deviation of the difference image.[37] If only one image is available, the noise can alternatively be measured directly from a large, uniform signal region as the standard deviation of the voxel values in that region.[38] The simplest way, however, is by estimating the noise from signal amplitude values of nonsignal regions,[38] because these are often easier to find than large homogeneous signal regions. The noise standard deviation is then given by 1.53 times the measured standard deviation of the background voxel values. The multiplication constant results from the fact that background noise obeys a Rayleigh distribution.[39,40] We employed the last method for noise estimation.

After the filtering process the gradient magnitude image is calculated for the next phase in the segmentation procedure. In order to save computation time one could argue that instead of filtering and afterwards edge detecting it would be more sensible to construct a robust edgedetector. This, however, is not true. The gain in SNR when filtering the original data is due to spatial averaging in all directions. On the other hand, only the response of an edge detector in the direction corresponding to a strong gradient increases the SNR. The response of the edge detector in the other directions does not increase the SNR; it even may lower the SNR.

The influence of the anisotropic diffusion filter on the segmentation results will be discussed in Experiments and Discussion.

SEGMENTATION

The actual semiautomatic segmentation procedure for 3D MR images consists out of three parts: (1) application of a 3D analogy of Vincent and Soille's watershed algorithm, (2) reduction of the oversegmentation by selectively merging neighboring catchment basins, and (3) interactive segmentation.

The first two steps are fully automatic. Some user interaction is required in the last part but the preceding ones will be shown to reduce this to a minimum.

Immersion-Based Watershed Algorithm

In the first part, the watersheds of the gradient magnitude of the MR data are calculated. By that, the gradient magnitude image is considered as a topographic relief where the brightness value of each voxel corresponds to a physical elevation. An efficient and accurate watershed algorithm was developed by Vincent and Soille,[26] who used an immersion-based approach to calculate the watersheds. The operation of their technique can simply be described by figuring that holes are pierced in each local minimum of the topographic relief. In the sequel, the surface is slowly immersed into a 'lake,' by that filling all the catchment basins, starting from the basin that is associated to the global minimum. As soon as two catchment basins tend to merge, a dam is built. The procedure results in a partitioning of the image in many catchment basins of which the borders define the watersheds.

Of all watershed transforms the immersion technique was shown to be the most efficient one in terms of edge detection accuracy and processing time.[27] For 3D implementation of the algorithm, it is assumed that the crest surfaces of the gradient magnitude of the 4D topographic relief correspond to structure surfaces of the original 3D data. We implemented dynamic linked lists to reduce memory requirements. Also, a 26-connected neighborhood was used that allows the water to flow in all directions. A 6-connected neighborhood could have been used instead to save computation time, but this goes along with a stronger oversegmentation and loss of watershed detection accuracy.

Merging of Volume Primitives

There is a severe drawback to the calculation of watershed images that is oversegmentation. The relevant object contours are lost in a sea of irrelevant ones. This is partly caused by random noise, inherent to MR data, which gives rise to additional local minima such that many catchment basins are further subdivided. If, however, an anisotropic diffusion filter (described in the Adaptive Anisotropic Diffusion Filter), is first applied to the original data, this oversegmentation can already significantly be reduced.

In a next step, the partitioning is additionally diminished by properly merging catchment basins. This is done by iteratively merging neighboring regions that have similar gray level distributions. The merging criterion is inspired from hypothesis testing where it is assumed that the population means are equal. Basic volume elements are assumed to be characterized by a Gaussian distribution. For small sample size ($n < 30$) a Student's t-test is most suited. The applied statistic is then given by:

$$t = \frac{\mu_1 - \mu_2}{\sigma\sqrt{\frac{1}{n_1} + \frac{1}{n_2}}} \text{ where } \sigma = \sqrt{\frac{n_1 S_1^2 + n_2 S_2^2}{n_1 + n_2 - 2}} \quad (8)$$

The variable t obeys a Student's t-distribution with $n_1 + n_2 - 2$ degrees of freedom, n_1 and n_2 denoting the number of pixels within the two populations. μ_1, μ_2 and S_1, S_2 are the estimated population means and standard deviations, respectively. Obviously, the smaller the t-value, the similar the distributions are.

The merging process proceeds as follows. The 3D MR data set is characterized by an array of structures where each structure describes one single basic volume element. The data of a structure contains the following information: the number of voxels, the voxel coordinates, the estimated mean gray value and standard deviation and an array containing the labels of the neighboring regions along with the corresponding value of the t statistic. The merging process starts by merging the smallest volume element with the most similar neighboring region; i.e., the region that gives the smallest t-value. During merging, all structure information of the two regions is combined and updated. Hereafter, the merging process is continued by again merging the smallest region with one of its neighbors. The process is stopped when half of the original number of regions is merged. From our experimental observations, further merging was found to degrade the posterior segmentation results too much in the sense that regions on the border of the cerebellum (object to be segmented) started to merge with neighboring regions from the surroundings. This criterion to stop the merging process depends, however, on the complexity of the segmentation task. In general, the stronger the edges surrounding the object to be segmented, the more regions that may be merged. Reduction of the number of small regions significantly favors the posterior interactive segmentation task, as will be elucidated below.

Interactive Segmentation

In the third part the actual object segmentation takes place. Subsequent 2D slices from the 3D data set are presented to the user. Each slice is accompanied by the basic volume elements which intersect the corresponding slice of the merged data. These volume elements are not visible to the user. The first slice is quickly segmented by manually activating the volume regions that belong to the object of interest through simple mouse clicking. This is done by drawing a contour around the region of interest, after which all interior regions are activated. All subsequent slices are consequently segmented as follows: the 'core' area of the previous slice (slice A), i.e., the area constituted of all previously activated regions except those lying at the border, is projected onto the next slice (slice B). All volume elements of slice B that intersect with this core area are automatically activated. Only the volume elements at the border of the core area of slice B are evaluated for activation. Volume elements at the border are automatically activated if a 'major part' is still contained in the segmentation result of slice A. The term 'major part' depends on the local deformation from one slice to another. If no deformation is observed the 'major part' is more than 50%. This percentage is made dependent on the local size change (growing or shrinking) and can range from 0 to 100%. Remark that automatic volume selection in this way does not require the object to be convex. The user contingently manually corrects the result of the automatic segmentation.

The adaptation from one slice to the next one is fully automatic when the local deformation is smaller than the average size of the basic volume elements. For this reason the merging process was designed to iteratively merge only the smallest regions. In this way, user interaction is minimal, mainly due to the efficient use of the 3D information.

EXPERIMENTS AND DISCUSSION

Materials

All data were generated on an MR apparatus (SMIS, Surrey, UK) with a horizontal bore of 8 cm, a field strength of 7 Tesla, and a maximal gradient strength of 0.2 Tesla/m. In all experiments a birdcage RF coil with a diameter of 32 mm was used. For each experiment a 3D spin echo (SE) pulse sequence was used (TE = 56 ms; TR = 1500 ms) with $FOV_x = FOV_y = 20$ mm and $FOV_z = 22$ mm. The acquisition matrix was: 256 × 128 × 128, which was zero-filled to obtain an image matrix of 256 × 256 × 256. The spatial resolution was $R_x = R_y = 78$ μm and $R_z = 86$ μm. For image processing a matrix of 120 × 220 × 150

Table 1. Accuracy of phantom volume quantization

Real object volumes (mm^3)	Volume 1 x-slicing (mm^3)	Volume 2 y-slicing (mm^3)	Volume 3 z-slicing (mm^3)	Segmentation error (%)
156	163	159	160	1.7
316	322	322	320	0.8
459	469	468	469	0.5
736	753	753	752	0.4

was chosen as a region of interest. All image processing was performed on an HP 720 workstation.

Phantom Object Data

After careful gradient calibrations, the proposed segmentation technique for volume quantization was in a first phase checked on images obtained from water-filled phantom objects. Although segmentation in this case is obvious, this test was performed to reveal possible biases in the volume quantization. The object volumes were chosen in the range of mouse brain volume: 156, 316, 459, and 756 mm^3. Each phantom volume was quantized three times: the 3D data was presented to the user by slicing in the x-, y-, and z-direction. Table 1 shows the true volumes of the phantom objects along with the measured volumes. The measured volumes reveal a systematic quantization error of about 2% while the intrinsic segmentation error is less than 1%, which indicates that the limiting factor in the volume quantization accuracy is due to the limited accuracy of the gradient calibration. As segmentation of our phantom object data was a very simple problem, it is believed that the segmentation procedure itself was extremely accurate. Furthermore, segmentation results of the phantom objects were statistically tested on their independence of slice direction. Thereby, ANOVA (analysis of variance) was used. It was found that the null hypothesis of equal volume means (between and within the slice directions) could not be rejected at a significance level of 0.05.

Mouse Data

To test the performance of the proposed segmentation technique on real data, we faced the problem of segmenting the cerebellum of mouse brains from 3D MR data. The proposed technique is very well suited for the cerebellum segmentation problem, first because the cerebellum structure is nontrivial, i.e., purely histogram-based segmentation techniques are useless. In addition, multispectral properties cannot be exploited to enhance the contrast between the cerebellum and the neighboring cerebrum, which would facilitate the posterior segmentation process. This is because the cerebellum has no significantly different MR relaxation characteristics than the cerebrum (both consist out of gray and white matter).

3D diffusion filter. The 3D raw MR data of the mouse head is first preprocessed with the anisotropic adaptive diffusion filter. Concerning the filtering neighborhood Ω, the following remarks can be made. First of all, the filtering range in one direction should be proportional to the spatial resolution in that direction. In our case, a cubic volume Ω was chosen as the raw data was zero filled to obtain a cubic data set. For optimal adaptation of the filtering kernel to the local structure, Ω must be as small as possible (e.g., a $3 \times 3 \times 3$ window). However the smaller Ω, the smaller the gain in SNR, which can be compensated by an iterative filtering scheme although this solution drastically elongates the processing time. As a compromise, we used a $5 \times 5 \times 5$ voxel window.

Figure 1 shows the effect of this operation. Figure 1a shows the midsagittal slice from the raw 3D MR data. Because of the large neighborhood, the filtering process results in a significant noise reduction as can be observed from the corresponding slice of the 3D output, shown in Fig. 1b. Beside a visual enhancement, the diffusion filter has also an important influence on the output of the immersion-based watershed algorithm. This can visually be appreciated from Fig. 2 where the watersheds of the same slice of respectively the original and the filtered data are shown. From Fig. 2a, an oversegmentation can clearly be observed: the data is subdivided in about 74000 homogeneous volume elements. By diffusion filtering, the number of basic volume elements in the 3D data set is reduced to less than one-third of the original number, as can be seen from Fig. 2b.

Merging. The result of the merging process is shown in Fig. 3, where Fig. 3a is a zoomed area from Fig. 2b. Although the number of volume elements was again halved because of the merging process, it might be hard to observe the differences between Fig. 3a and Fig. 3b. This is because only the smallest regions were considered for merging. However, the merging operation significantly diminishes the posterior user interaction time.

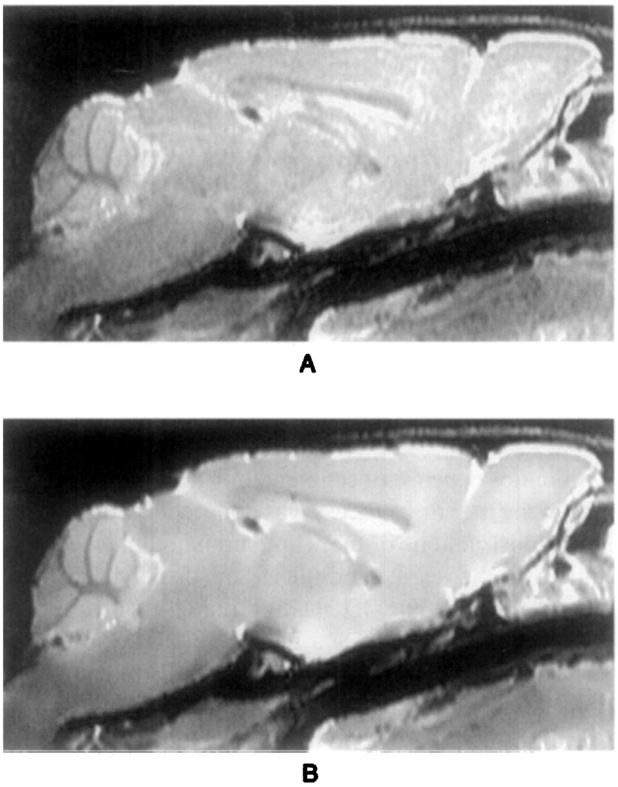

Fig. 1. Result of 3D adaptive anisotropic diffusion filter.

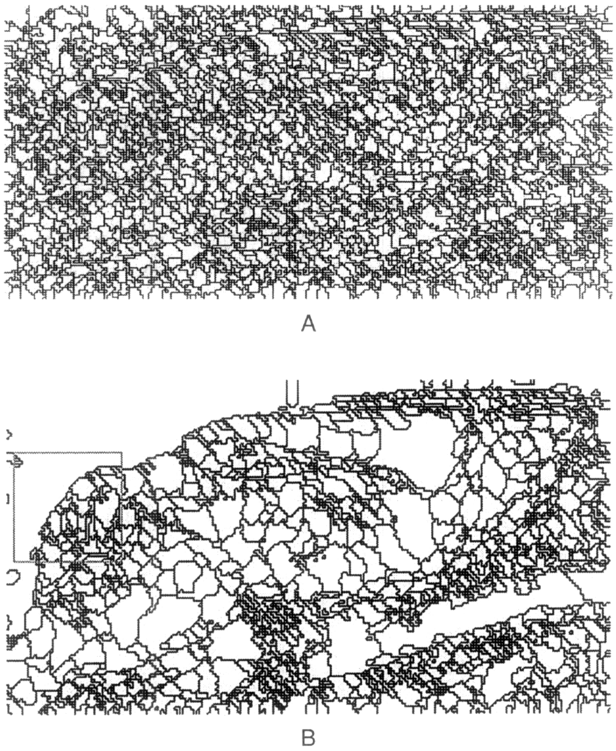

Fig. 2. Watershed transforms of raw, filtered, and merged data.

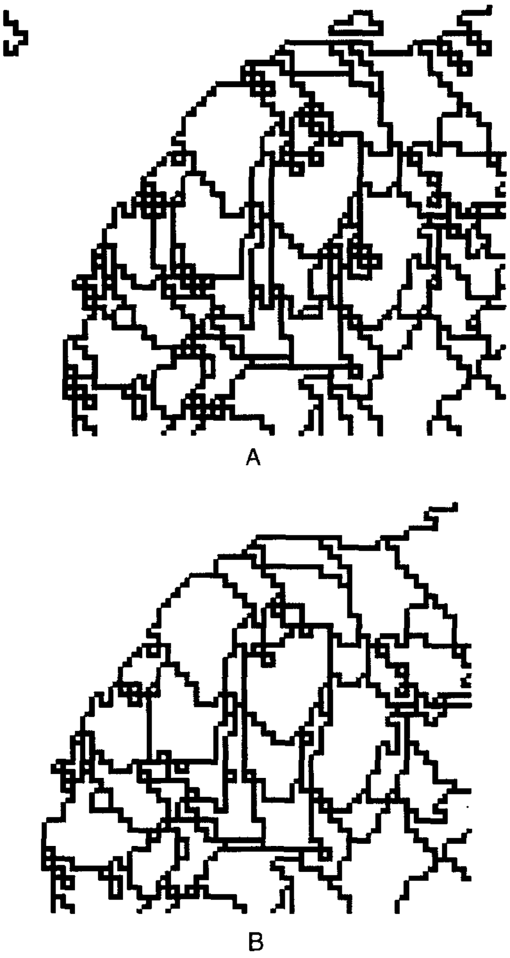

Fig. 3. Result of the merging process.

The effect on the size of the volume elements is demonstrated in Fig. 4. Figure 4a shows the histogram of the region sizes for the raw, filtered, and merged data. From this figure it is clear that many small regions are merged with neighboring ones. Figure 4b shows the cumulative volume histogram. Every curve finally converges to the total volume of the region of interest.

Interactive segmentation. The result from the full automatic preprocessing steps is presented to the user for manual segmentation. With a few mouse clicks on the first slice, the cerebellum is extracted from the rest of the brains. This is not done by activating each single region from the cerebellum separately but by selecting a region of interest in which all volume elements are automatically activated. Starting from this slice the segmentation process is proceeded, hereby fully exploiting the 3D information of the previously segmented slice. In Fig. 5 the segmented result of the midsagittal slice is shown. For clarity, only the border

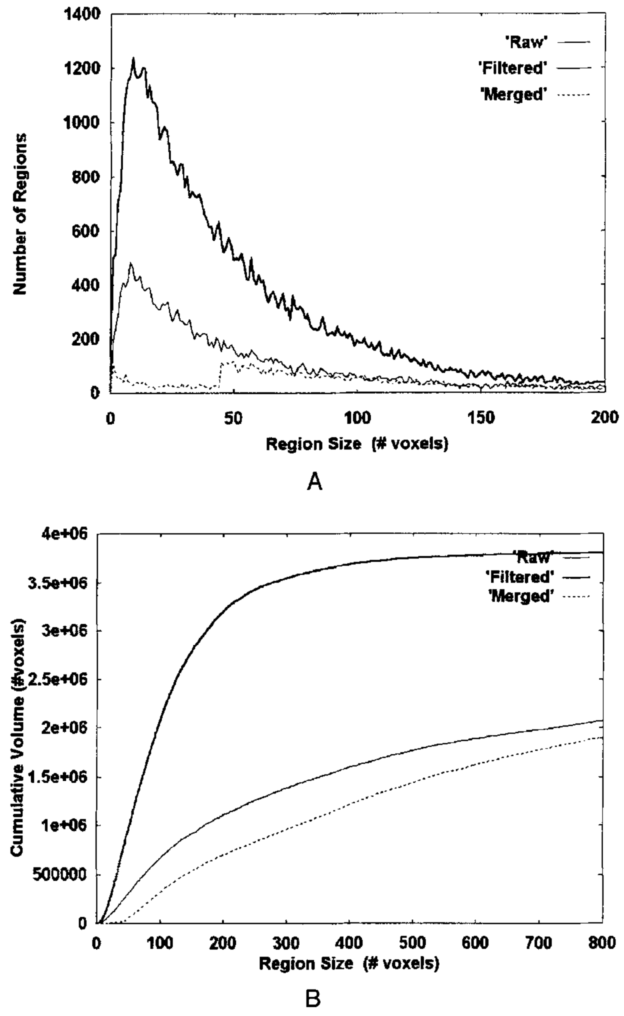

Fig. 4. Effect of filtering and merging on the size of the volume elements.

of the segmented volumes in the slice is shown as a white border.

Volume quantization. Numerical results of the segmentation process are summarized in Table 2. As a consequence of the diffusion filter, the number of manual interactions (mouse clicks) is significantly reduced. Further iteratively merging volume primitives halves this number along with the interaction time. However, reduction of user interaction time goes along with minor expense of segmentation accuracy. For this reason the merging process was not proceeded. Finally, 3D reconstructions of the whole brain and the cerebellum from the segmented slices are displayed in Fig. 6a and Fig. 6b. The 3D shading renderings were created using Interactive Data Language (IDL) software.

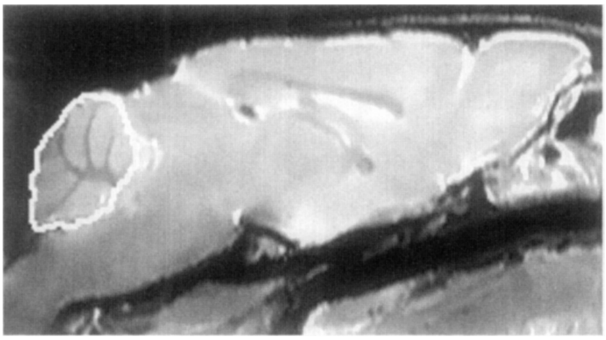

Fig. 5. Cerebellum extraction via volume element selection.

Slicing of the total mouse brains in different directions led to results, equal within 1%; the volume quantifications for the cerebellum were equal within 3%. The operator variability was about 3%. Although gradient calibration limitations must also be taken into account, these results are satisfying in comparison to the volume measurements obtained from invasive techniques (slicing of the fixated mouse head) where errors of more than 10% are common. This is mainly due to the fixation process, which leads to volume changes (shrinking or expansion). Similar errors are introduced when cutting the cerebellum from the rest of the brain and measuring the volume after immersion into a fluid. In addition, the proposed noninvasive segmentation techniques for volume quantization has this advantage over the invasive method that in vivo studies can be performed, which allows the study of volume dynamics.

Segmentation performance. 3D adaptive anisotropic diffusion filtering with a 5 × 5 × 5 window took about 14 min. Calculation of the 3D watershed image took less than 4 min. Merging volume primitives required 9 min. Hence, all fully automatic preprocessing steps were completed within half an hour. Finally, the user

Table 2. Segmentation results of mouse brain segmentation

Method	Number of volume elements	Number of man. interac. per slice	Total brain volume (mm^3)	Cerebellum volume (mm^3)
Raw data	74053	17.1	559 ± 1	65.4 ± 1.4
After diff.filtering	23203	5.4	560 ± 2	64.0 ± 1.9
After merging	11601	2.6	559 ± 2	63.7 ± 2.1

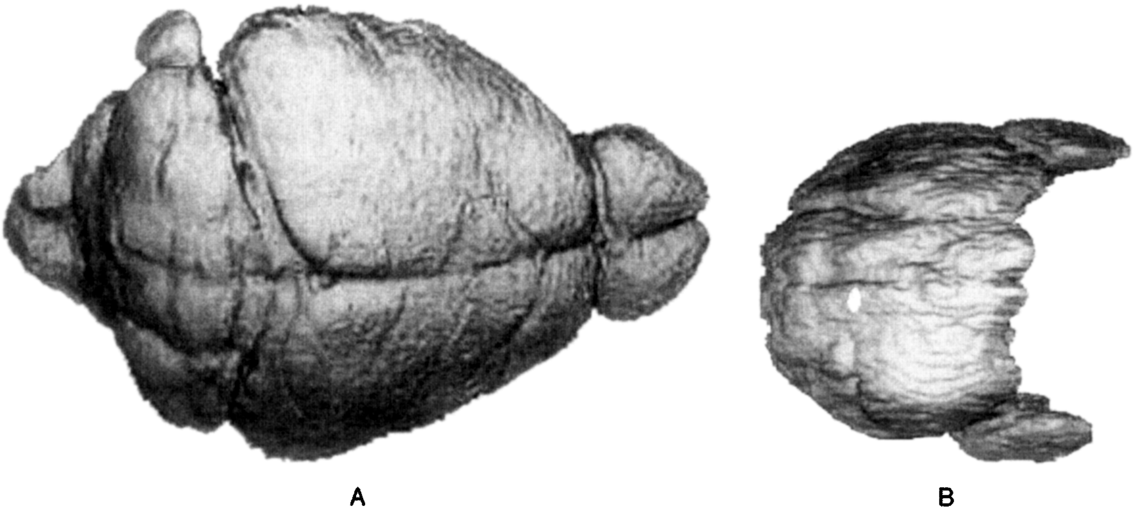

Fig. 6. 3D reconstructions of the segmented objects.

interaction time to extract the cerebellum from the rest of the image took about 2.5 s per slice. The interactive segmentation for the cerebellum was completed within 7 min. The total brain was segmented within 11 min. Although far more volume elements were involved in the segmentation of the total brain, segmentation was less complex as the contrast between the total brain and the surroundings was higher. In general, the speed of segmentation depends very much on the clearness of the object boundary, and in minor way, on the shape of the object.

Concerning the performance of the proposed segmentation procedure, some general conclusions can be drawn. The method obviously works best when the object of interest is delineated by a strong contour in the data. Furthermore, the performance depends on the deformation from one slice to the other: automation increases when the local deformation is smaller than the average size of a basic volume element. If this is a problem, a possible solution might be zero filling of the raw data, thereby extrapolating between subsequent slices. Homogeneity within the object or convexity is not required. The influence of random noise on the segmentation performance can be combatted as described in this article. However, segmentation results will degrade when structured noise is present due to magnetic field inhomogeneities, object movement, etc.

CONCLUSION

In conclusion, we proposed a semiautomatic 3D segmentation technique grounded on the immersion-based watershed algorithm. We showed that preprocessing the data with a 3D adaptive anisotropic diffusion filter has a positive impact on the segmentation results. A posteriori merging of basic volume primitives additionally reduces the user interaction time. The proposed segmentation technique is successfully used to extract quantitative volume information from 3D images of in vitro mouse cerebella. It has proved to be superior in comparison with existing invasive methods.

REFERENCES

1. Clarke, L.P.; Velthuizen, R.P.; Camacho, M.A.; Heine, J.J.; Vaidyanathan, M.; Hall, L.O.; Thatcher, R.W.; Silbiger, M.L. MRI segmentation: Methods and applications. Magn. Reson. Imaging 13:343–368; 1995.
2. Suzuki, H.; Toriwaki, J. Automatic segmentation of head MRI images by knowledge guided thresholding. Comput. Med. Imaging Graphics 15:233–240; 1991.
3. Lim, K.O.; Pfefferbaum, A. Segmentation of MR brain images into cerebrospinal fluid spaces, white and gray matter. J. Comput. Assist. Tomogr. 13:588–593; 1989.
4. Kundu, A. Local segmentation of biomedical images. Comput. Med. Imaging Graphics 14:173–183; 1990.
5. Bomans, M.; Hohne, K.H.; Tiede, U.; Riemer, M. 3D segmentation of MR images of the head for 3D display. IEEE Transact. Med. Imaging 9:177–183; 1990.
6. Ashtari, M.; Zito, J.L.; Gold, B.I.; Lieberman, J.A.; Borenstein, M.T.; Herman, P.G. Computerized measurement of brain structure. Invest. Radiolol. 25:798–805; 1990.
7. Dellepiane, S. Image segmentation: Errors, sensitivity and uncertainty. Proc. 13th IEEE-Eng. Med. Biol. Soc. 13:253–254; 1994.
8. Gerig, G.; Martin, J.; Kikinis, R.; Kubler, O.; Shenton, M.; Jolesz, F.A. Unsupervised tissue type segmentation of 3D dual-echo MR head data. Image Vision Comput. 10:346–360; 1992.

9. Geman, S.; Geman, D. Stochastic relaxation, Gibbs distribution and the bayesian restoration of images. IEEE Transact. Pattern Anal. Machine Intell. 6:721–741; 1984.
10. Pappas, T.N. An adaptive clustering algorithm for image segmentation. IEEE Transact. Signal Proc.; SP-40:901–914; 1992.
11. Hall, L.O.; Bensaid, A.M.; Clarke, L.P.; Velthuizen, R.P.; Silbiger, M.S.; Bezdek, J.C. A comparison of neural network and fuzzy clustering techniques in segmenting magnetic resonance images of the brain. IEEE Transact. Neural Net. 3:672–682; 1992.
12. Bezdek, J.C.; Hall, L.O.; Clarcke, L.P. Review of MR image segmentation techniques using pattern recognition. Med. Phys. 20:1033–1048; 1993.
13. Bellon, E.M.; Haacke, E.M.; Coleman, P.E.; Sacco, D.C.; Steiger, D.A.; Gangarosa, R.E. MR artefacts: A review. Am. J. Roentgenol. 147:1271–1281; 1986.
14. Wang, Y.; Lei, T. Statistical analysis of MR imaging and its applications in image modeling. Proceedings of the IEEE international conference on image processing and neural networks, vol. I. 1994:866–870.
15. McVeigh, E.R.; Henkelman, R.M.; Bronskil, M.J. Noise and filtration in magnetic resonance imaging. Med. Phys. 12:586–591; 1985.
16. Parker, D.L.; Gullberg, G.T.; Frederick, P.R. Gibbs artefact removal in magnetic resonance imaging. Med. Phys. 14:640–645; 1987.
17. Fuderer, M. The information content of MR images. IEEE Transact. Med. Imaging 7:368–380; 1988.
18. Daubechies, I. Orthonormal bases of compactly supported wavelets. Commun. Pure Appl. Math. 41:909–996; 1988.
19. Weaver, J.B.; Xu, Y.; Healy, D.M.; Cromwell, L.D. Filtering noise from images with wavelet transforms. Magn. Reson. Med. 21:288–295; 1991.
20. Saint-Marc, P.; Chen, J.S.; Medioni, G. Adaptive smoothing: A general tool for early vision. IEEE Transact. Pattern Anal. Machine Intell. 12:629–639; 1990.
21. Ying, K.; Clymer, B.; Schmalbrock, P. Adaptive filtering processing of magnetic resonance images. In: Book of Abstracts: Second Annual Meeting of the Society of Magnetic Resonance in Medicine. Berkeley, CA; 1994:803.
22. Perona, P.; Malik, J. Scale space and edge detection using anisotropic diffusion. IEEE Transact. Pattern Anal. Machine Intell. 12:629–639; 1990.
23. Gerig, G.; Kubler, O.; Kikinis, R.; Jolesz, F.A. Nonlinear anisotropic filtering of MRI data. IEEE Transact. Med. Imaging 11:221–232; 1992.
24. Yang, G.Z.; Burger, P.; Firmin, D.N.; Underwood, S.R. Structure adaptive anisotropic filtering for magnetic resonance image enhancement. Proceedings of CAIP; 1995:384–391.
25. Weickert, J. Multiscale texture enhancement. Proceedings of CAIP; 1995:230–237.
26. Vincent, L.; Soille, P. Watersheds in digital spaces: An efficient algorithm based on immersion simulations. IEEE Transact. Pattern Anal. Machine Intell. 13:583–593; 1991.
27. Hagyard, D.; Razaz, M.; Atkin, P. Analysis of watershed algorithms for greyscale images. Proceedings of the IEEE International Conference on Image Processing, vol. 3; 1996:41–44.
28. Maes, F.; Vandermeulen, D.; Suetens, P.; Marchal, P. Automatic image partitioning for generic object segmentation in medical images. Proceedings of the 14th International Conference on Image Processing in Medical Imaging; 1995:215–226.
29. Cover, T.M.; Thomas, J.A. Elements of Information Theory. New York: John Wiley and Sons; 1991.
30. Rissanen, J. Minimum description length principle, vol. 5. In: Encyclopaedia of Statistical Sciences. New York: Wiley; 1987.
31. Leclerc, Y.G. Constructing simple stable descriptions for image partitioning. Int. J. Comput. Vision 3:73–102; 1989.
32. Silverman, B.W. Density Estimation for Statistics and Data Analysis. London: Chapman and Hall; 1986.
33. Reiss, A.L.; Freund, L.; Tseng, J.E.; Joshi, P.K. Neuroanatomy in fragile X females: The posterior fossa. Am. J. Hum. Genet. 49:279–288; 1991.
34. Courchesne, E.; Yeung-Courchesne, R.; Press, G.A.; Hesselink, J.R.; Jernigan, T.L. Hypoplasia of cerebellar vermal lobules VI and VII in autism. New Engl. J. Med. 318:1349–1358; 1988.
35. The Dutch–Belgian Fragile X Consortium. FMR1 knockout mice: A model to study fragile X mental retardation. Cell 78:23–33; 1994.
36. Murphy, B.W.; Carson, P.L.; Ellis, J.H.; Zhang, Y.T.; Hyde, R.J.; Chenevert, T.L. Signal-to-noise measures for magnetic resonance imagers. Magn. Reson. Imaging 11:425–428; 1993.
37. Sano, R.M. Nema standards. Performance standards for clinical magnetic resonance systems. In: R.L. Dixon (Ed). MRI acceptance testing and quality control—The role of the clinical medical physicist. Madison, WI: Medical Physics Publishing Company; 1988:185–189.
38. Kaufman, L.; Kramer, D.M.; Crooks, L.E.; Ortendahl, D.A. Measuring signal-to-noise ratios in MR imaging. Radiology 173:265–267; 1989.
39. Henkelman, R.M. Measurement of signal intensities in the presence of noise in MR images. Med. Phys. 12:232–233; 1985.
40. Bernstein, M.A.; et al. Improved detectability in low signal-to-noise ratio magnetic resonance images by means of phase-corrected real construction. Med. Phys. 12:813–817; 1989.